

Article

Robust Impact Effect and Super-Lyophobic Reduced Galinstan on Polymers Applied for Energy Harvester

Husheng Chen, Shilong Hu, Yuan Jin, Aibing Zhang *, Licheng Hua, Jianke Du * and Guangyong Li *

Smart Materials and Advanced Structure Laboratory, School of Mechanical Engineering and Mechanics, Ningbo University, Ningbo 315211, China

* Correspondence: zhangaiqing@nbu.edu.cn (A.Z.); dujianke@nbu.edu.cn (J.D.); liguangyong@nbu.edu.cn (G.L.)

Abstract: In this paper, we present a novel reduced Galinstan-based microfluidic energy harvester, which can converse kinetic energy to electricity from an arbitrary vibration source. Firstly, the wetting behaviors of reduced Galinstan are performed, which shows a robust impact effect on polymer substrates. Moreover, the electric circuit model of the reduced Galinstan-based energy harvester is made and discussed by the use of the EDLCs (electrical double layer capacitors). After modeling, the microfluidic energy harvester with coplanar microfluidic channels is designed and fabricated. Finally, the performance of the microfluidic energy harvester is investigated, which can harvest multi-direction vibration energy. The experiment results demonstrate that the novel reduced Galinstan-based microfluidic energy harvester is suitably and uniquely applied in a complex vibration environment.

Keywords: liquid metal; reduced Galinstan; impact effect; energy harvester



Citation: Chen, H.; Hu, S.; Jin, Y.; Zhang, A.; Hua, L.; Du, J.; Li, G. Robust Impact Effect and Super-Lyophobic Reduced Galinstan on Polymers Applied for Energy Harvester. *Polymers* **2022**, *14*, 3633. <https://doi.org/10.3390/polym14173633>

Academic Editors: Sheng Hsiung Chang and Hsin-Ming Cheng

Received: 13 July 2022

Accepted: 29 August 2022

Published: 2 September 2022

Publisher's Note: MDPI stays neutral with regard to jurisdictional claims in published maps and institutional affiliations.



Copyright: © 2022 by the authors. Licensee MDPI, Basel, Switzerland. This article is an open access article distributed under the terms and conditions of the Creative Commons Attribution (CC BY) license (<https://creativecommons.org/licenses/by/4.0/>).

1. Introduction

Due to the unlimited power which can be scavenged from the ambient environment, the energy harvesting technology has been regarded as the most potential method for powering the sense nodes in various WSN (wireless sensor network) applications (structural monitoring, traffic accident precaution and military detection, etc.). In the last decade, various energy harvesters have been developed based on diverse energy conversion principles, such as piezoelectric, electromagnetic, and electrostatic phenomenon [1–8].

Recently, a new type of microfluidic energy harvester has drawn more attention due to its high power density. According to Krupenkin et al., electrical power was generated by squeezing the liquid droplets between vibrating plates based on the reverse electrowetting principle [9]. Moon et al. found that electrical energy generation is achieved by mechanically modulating the water droplet without an external bias voltage source [10–14]. The water-TENG (triboelectric nano generator) was intensively studied due to its great potential for harvesting the energy from water triboelectrification [15–25]. Compared to the conventional method, the power density was largely improved. The working mechanism of the microfluidic energy harvester can be represented with EDLCs (electrical double layer capacitors) based on the change in capacitance. This capacitance change depends largely on the interface area variation between the liquid and the conducting plate. However, the liquid media in this approach is the water in nature, which has a small area change when contacting liquid and the conducting plate due to its low surface tension and weak hydrophobic properties. Furthermore, water always evaporates in the open environment and cannot work at relatively high or low temperatures (such as $>100\text{ }^{\circ}\text{C}$ or $<0\text{ }^{\circ}\text{C}$). Additionally, for the energy harvester based on nature water or ionic liquid, the available vibration source is limited in a single vertical direction due to the open structure.

Liquid metal is a pure metal or an alloy with a very low melting point and is in liquid phase at room temperature (or near room temperature), as shown in Table S1 of

the Supplementary Material. Mercury is the most well-known liquid metal, which can replace ionic liquid and water in a microfluidic energy harvester. Yang et al. proposed an energy harvester using mercury droplets and ionic liquid marbles rolling across a charged electret film [13,26,27]. Nevertheless, its toxicity and higher vapor pressure pose a challenge for its widespread applications. Gallium-based liquid metal alloy has emerged as a replacement of previously employed toxic mercury due to its non-toxicity [28,29]. Some typical gallium-based liquid metals include EGaIn (eutectic gallium-indium) and Galinstan (Ga-In-Sn alloy). Dickey and Kim et al. proposed a liquid metal-based energy harvester that can convert mechanical energy to electrical energy by deforming Galinstan droplets [9,30,31]. The core idea of the energy harvester largely originated from the position and shape change of Galinstan. Power generated using Galinstan can be maximized by increasing the capacitance of the liquid–solid interface [32]. Thus, the easy manipulation of Galinstan is very important in efficient working of the liquid metal-based energy harvester. However, Galinstan is easily oxidized in air the environment and forms an oxide shell on its surface. It behaves more similar to gel rather than true liquid, and adheres to almost any solid surface [33–41]. This oxide shell is solid and remains elastic unless it experiences a yield stress, which presents a significant sticky problem for increasing the capacitance of the liquid–solid interface. Luckily, the oxidation layer of Galinstan can be removed by hydrochloric acid or sodium hydroxide solution that remains in the true liquid phase [42–45].

In this paper, the oxidation layer of Galinstan is first removed by using reduction technology. The reduced Galinstan shows super-lyophobic behaviors on non-metal substrates, which can increase the capacitance of the liquid–solid interface. After characterizing the lyophobic behaviors, an EDLC-based microfluidic energy harvester with reduced Galinstan is designed and fabricated to collect energy from an arbitrary vibration source. The novel device can not only overcome the problems of mercury toxicity and the easy oxidation of Galinstan, but also avoids the evaporation of water in the air environment.

2. Results and Discussion

2.1. Wetting Behaviors of Galinstan

2.1.1. Wetting Behaviors of Oxidized Galinstan

The liquid droplet shows different wetting behaviors when it contacts with the various substrates. Before analyzing the impact effect of reduced Galinstan, its wetting behaviors are characterized. As is well known, the contact angle is an experimentally observable quantity that describes the wetting property of a liquid in contact with a solid surface and surrounded by another immiscible fluid (most commonly a gas). Classical Young's equation (Equation (1)) is widely used to describe the contact angle of a liquid droplet on a flat solid surface:

$$\cos \theta = \frac{\gamma_{SG} - \gamma_{SL}}{\gamma_{LG}} \quad (1)$$

where θ is the contact angle; γ_{SL} is the surface tension of solid–liquid interfaces; γ_{LG} is the surface tension of liquid–gas interfaces; and γ_{SG} is the surface tension of solid–gas interfaces.

In order to analyze the wetting behavior of oxidized Galinstan, the contact angles of the oxidized Galinstan droplet (OGD) on various substrates (Glass, PDMS, Au and Cu) are measured as shown in Figure 1. Galinstan (~8 μL) is dropped on the Glass, PDMS, Au and Cu substrate surface using a syringe, respectively. The tip formed from the dispensing of the droplet does not relax, as shown in Figure 1. This is attributed to the oxidation of the surface of Galinstan. Here, the droplet contact angle measurements are performed using a charge-coupled device (CCD) camera (30 frames/second), along with image processing technique. The static contact angles of the OGD on these abovementioned substrate surfaces are in the range from ~125° to ~130°. Even after 2.5 h, the static contact angles almost have no changes, because the oxidation layer on the Galinstan droplet is similar to a shell, which restricts its further spreading on the substrate surface.

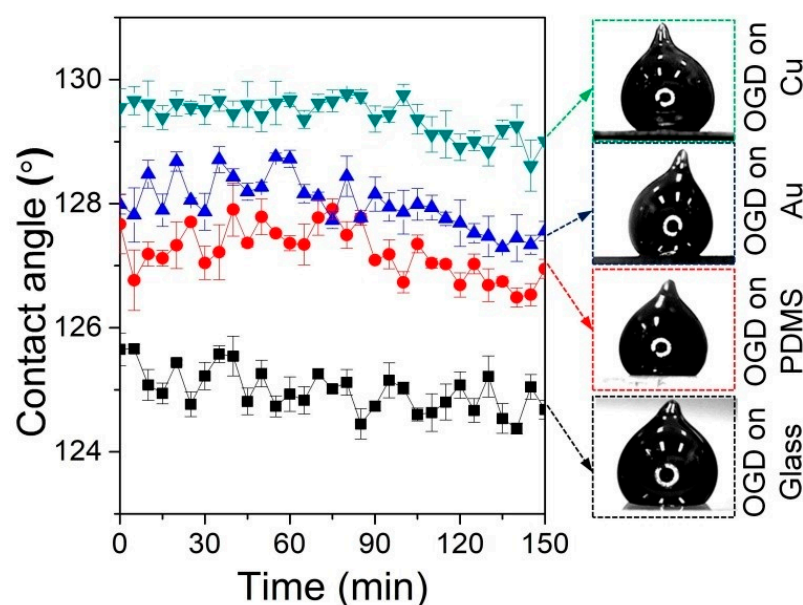


Figure 1. The static contact angles of the OGD on various substrates (Glass, PDMS, Au and Cu) as a function of time.

Along with the static contact angle, in order to further investigate the wetting behavior of oxidized Galinstan, the dynamic contact angle of the OGD is particularly important. Advancing and receding contact angles are obtained by adding and withdrawing Galinstan from a droplet with the dispensing needle. Galinstan is continuously supplied to the droplet through the needle until it reaches the maximum volume of 40 μL . After that, Galinstan is withdrawn from the droplet. The addition or withdrawal rate of Galinstan is 16 $\mu\text{L}/\text{s}$. The contact angle changes are recorded by the CCD camera (Model JHSM300m). Advancing and receding contact angles of the OGD on various substrates (Glass, PDMS, Au and Cu) are also obtained, as shown Figure 2. We can observe that the advancing angles are almost same ($\sim 155^\circ$) for various substrates. This can be explained by assuming that the oxidation layer of Galinstan droplet is replaced by non-oxidized Galinstan, and hence behaves more similar to true liquid with increasing the volume of Galinstan droplet. The receding angles are even lower than 10° before the liquid disconnection during the suction back (shown in the Supplementary data, Figure S2). There is residual Galinstan on the various substrates, as shown in Figure 2(a12,b4,c4,d4). Because the surface of Galinstan is instantly oxidized in ambient conditions and it behaves more similar to gel rather than true liquid, it adheres to almost any solid surface. The suction force cannot overcome the adhesive force during the receding process. The mechanism of the liquid metal-based energy harvester is largely originated from the position and shape change of Galinstan. Power density using Galinstan can be maximized by increasing the capacitance of the liquid–solid interface. As shown in Figure 2, the liquid–solid interfacial area of OGD on the substrate changed almost nothing in receding step. Therefore, the surface of OGD should be modified to make it be in true liquid phase for increasing the capacitance of the liquid–solid interface, which can increase the power density of the liquid metal-based energy harvester [30–32].

2.1.2. Wetting Behaviors of Reduced Galinstan

The static contact angles of the RGD (reduced Galinstan droplet) on various substrates (PDMS, Au, Cu and Zn (zinc)) are tested, as shown in Figure 3. When the oxidation layer on Galinstan surface is reduced using HCl vapor, the static contact angle of the RGD ($\sim 8 \mu\text{L}$) on PDMS substrate reaches to $\sim 155^\circ$, as shown in Figure 3a. The static contact angle of the RGD ($\sim 8 \mu\text{L}$) on metal substrate is only $\sim 6^\circ$, as shown in Figure 3d. As observed in Figures S1 and S2 of Supplementary Material, the RGD fully wets the Au layer in $\sim 0.5 \text{ s}$.

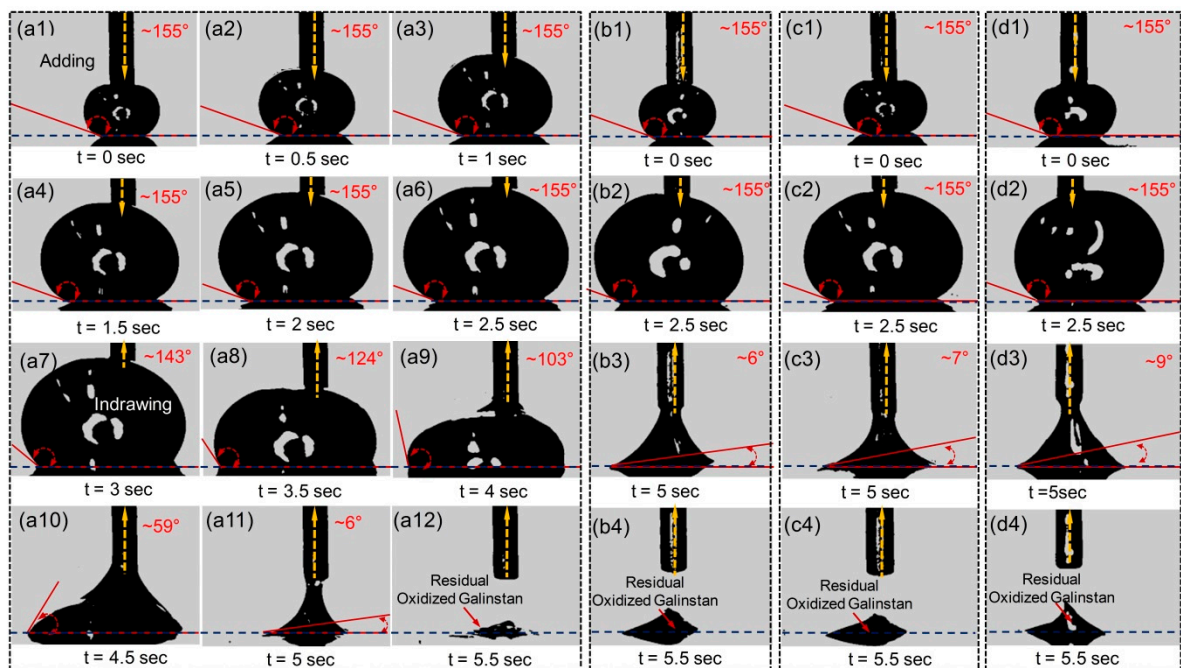


Figure 2. Photographs of advancing and receding angles of the OGD on (a) Glass, (b) PDMS, (c) Au and (d) Cu substrate.

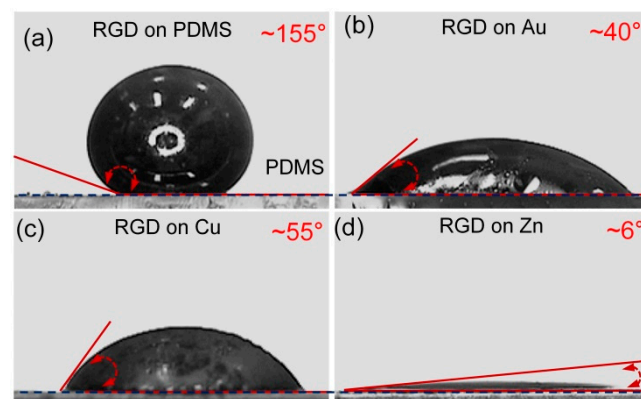


Figure 3. Photographs of static contact angles of the RGD on various substrates ((a) PDMS, (b) Au, (c) Cu and (d) Zn).

Using the same measurement process as before, receding and advancing contact angles of the RGD on non-metal and metal substrates (PDMS and Au) are obtained as shown in Figure 4. As seen from Figure 4a, it is found that reduced Galinstan has super-lyophobic behaviors, with smaller contact angle hysteresis of $\sim 17^\circ$ (difference value of receding angle $\sim 138^\circ$ and advancing angle $\sim 155^\circ$) when it is dropped on the non-metal substrate (PDMS). For the metal substrate (Au), the advancing angle of the RGD is $\sim 40^\circ$ to $\sim 60^\circ$ and the receding angle is only $\sim 7^\circ$ before the liquid disconnection during the suction back, which shows super-lyophilic behaviors.

2.1.3. Impact Effect of Reduced Galinstan

After investigation of the wetting behaviors, the impact effect of the RGD is performed, as shown in Figure 5. Here, a high speed CCD camera (1200 images/s) is used for recording the droplets during the free falling and impacting. The impact effect of the RGD is analyzed when it is released from a height of 20 mm and impacts on the Au and PDMS surface. Figure 5a shows the RGD falling and impacting on the PDMS surface. During its free falling, the RGD maintains a spherical shape. When it is impacting on the PDMS surface,

the RGD presents a crown-like rim shape. When the RGD rebounds from the PDMS surface, it recovers its spherical shape seen in Video S1 of the Supplementary Material. Figure 5b shows the RGD falling and impacting on the Au surface. The RGD maintains its almost spherical shape throughout the free fall. When it is impacting on the Au surface, we can again observe a crown-like rim shape RGD. The conical shape and the hemispherical shape alternately appear. At last, the RGD shows a hemispherical shape. Compared with the PDMS surface, there is no rebound on the Au surface, as seen in Video S2 of the Supplementary Material. The reason is that the reduced Galinstan shows super-lyophilic behaviors on metal substrates and super-lyophobic behaviors on non-metal substrates, as shown in Figure 4.

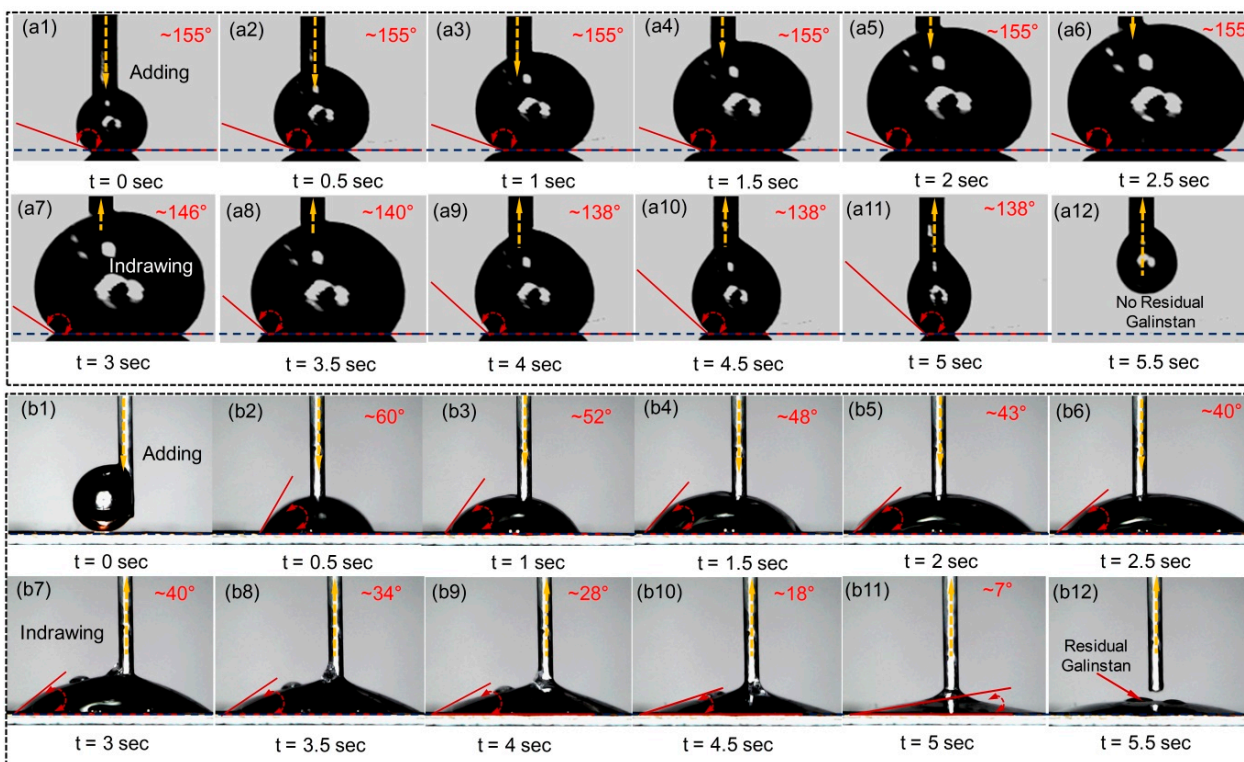


Figure 4. Photographs of advancing and receding angles of the RGD on (a) PDMS and (b) Au substrate.

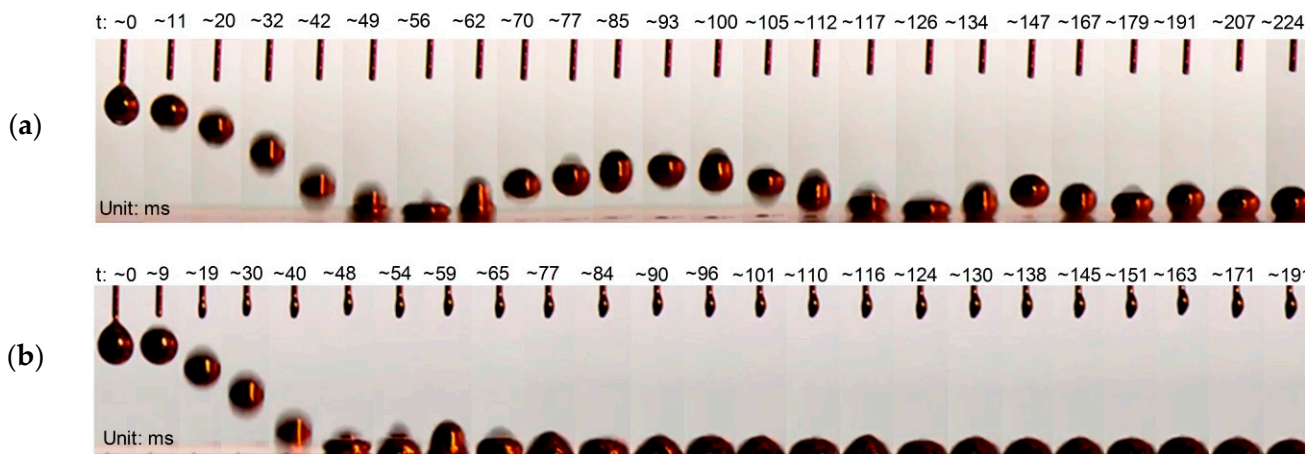


Figure 5. Sequential images of the RGD after being released from a syringe needle, falling and impacting on (a) PDMS and (b) Au surface.

2.2. Microfluidic Energy Harvester Application

2.2.1. Electric Circuit Modeling of the Reduced Galinstan-Based Energy Harvester

Figure 6 shows a schematic diagram of the EDLC-based microfluidic energy harvester using the reduced Galinstan. A RGD is positioned between two parallel conducting plates. The EDLC, formed on the two interfacial areas between the droplet and conducting plates, are continuously charged and discharged during the impact from each other. When the electron passes through the load resistance R_L , the electrical current can be observed. The contact area A_T and A_B between reduced Galinstan and the plate changes appreciably during each impacting period. The capacitances (C_T , C_B) of both top and bottom EDLC can be presented as:

$$C_T(t) \cong \frac{\epsilon_0 \epsilon_d}{\lambda_D} A_T(t) \tag{2}$$

$$C_B(t) \cong \epsilon_0 A_B(t) \left(\frac{d}{\epsilon_p} + \frac{\lambda_D}{\epsilon_d} \right)^{-1} \cong \frac{\epsilon_0 \epsilon_p}{d} A_B(t) \tag{3}$$

where ϵ_0 is the vacuum permittivity, d is the thickness of the dielectric material coated on the top conductive plate, λ_D is the thickness of the electrical double layer, ϵ_p is the dielectric constant of the dielectric material, and ϵ_d is the dielectric constant of HCl solution. As $d/\epsilon_p \gg \lambda_D/\epsilon_d$, the λ_D/ϵ_d of Equation (2) can be justifiably ignored.

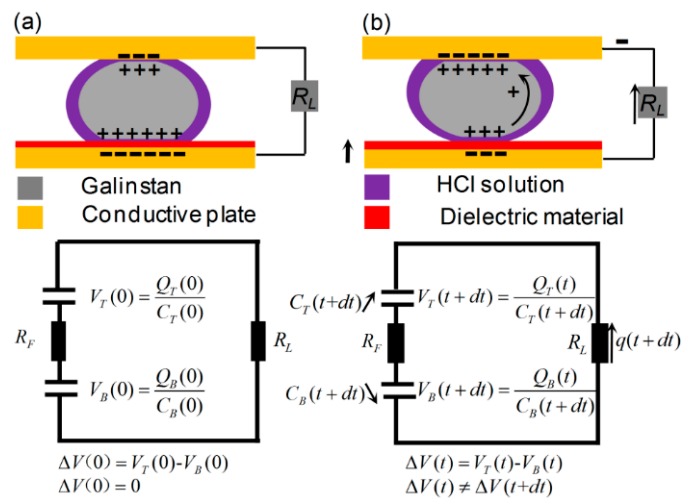


Figure 6. The equivalent electrical circuit at the very moment (a) when the EDLC system is in a state of equilibrium and (b) when the EDLCs system is in state of non-equilibrium.

As shown in Figure 6a, $V_T(t)$ ($Q_T(t)$) and $V_B(t)$ ($Q_B(t)$) are the voltages (charges stored) on C_T and C_B at time $t = 0$, respectively. R_F is the electrical resistance across the liquid droplet. When the EDLCs system is in a state of equilibrium, $V_T(0) = V_B(0)$ and no current flows.

Figure 6b shows the electrical circuit at the very moment when the EDLCs system is in a state of non-equilibrium after the vibration commences at $t = 0$. In this case, as the contact area A_B (A_T) at the bottom (top) plate decreases (increases), C_B decreases and C_T increases. As $C_B(t)$ ($C_T(t)$) decreases (increases) in time, the voltage $V_B(t)$ ($V_T(t)$) decreases (increases), which generates a voltage difference, $\Delta V(t) = V_B(t) - V_T(t)$ and $\Delta V(t) \neq \Delta V(t+dt)$. Therefore, the electric circuit can be explained by using the following equation:

$$\begin{aligned} (R_L + R_F) \frac{q(t+dt) - q(t)}{dt} &= V_B(t) - V_T(t) \\ &= \frac{Q_B(t)}{C_B(t+dt)} - \frac{Q_T(t)}{C_T(t+dt)} \end{aligned} \tag{4}$$

Here, $q(t + dt) - q(t)$ is the increment (decrement) of charge in the top (bottom) EDLCs in time dt . Thus, the voltage drop on R_L is:

$$V_L(t) = \lim_{dt \rightarrow 0} \frac{q(t + dt) - q(t)}{dt} R_L \quad (5)$$

2.2.2. Reduced Galinstan-Based Energy Harvester

In order to realize the conversion from kinetic energy to electricity, the EDLC- and reduced Galinstan-based energy harvester was designed and fabricated, as shown in Figure 7. After fabrication, the experiment setup comprising of a function generator, voltage amplifier, shaker and oscilloscope is used to characterize behaviours of the energy harvester, as shown in Figure 8. Simple harmonic vibration is the simplest and most basic form of vibration. The output voltage peak, ~ 80 mv, was achieved by squeezing the liquid droplets between vibrating plates with 10 Hz sine wave signals [10]. In order to conveniently verify the reliability of the developed energy harvester, the sine wave was chosen as a vibration source. The voltage (open circuit) is measured as shown in Figure 9. Figure 9a shows the output voltage of the energy harvester after a 2 Hz sine wave excitation when it vibrates in the vertical direction (Video S3 of the Supplementary Material). Moreover, output voltage of the energy harvester vibrating in the horizontal direction is shown in Figure 9b and Video S4 of the Supplementary Material. In order to further investigate the performance of the reduced Galinstan-based microfluidic energy harvester, the output voltage peak of energy harvester is tested when the applied excitation wave frequency is increased. Figure 9c shows the output voltage peak of energy harvester as a function of the excitation wave frequency. After applying a 2 Hz sine wave, the output voltage peak went up to ~ 400 mv. When the R_L is $1 \text{ M}\Omega$, the power density is about 40 mW m^{-2} . The comparisons of the liquid metal-based energy harvester discussed in previous studies are shown in Table S2 of the Supplementary Material [9,30,31]. Vibration occurs widely in nature, for example, in the form of human walking, ocean waves, and vibration of mechanical systems. Typically, these vibrations are of a low frequency and multidirectional [27,46,47]. Therefore, the developed energy harvester is suitable for low frequency vibration energy harvesting and uniquely applied in a complex vibration environment.

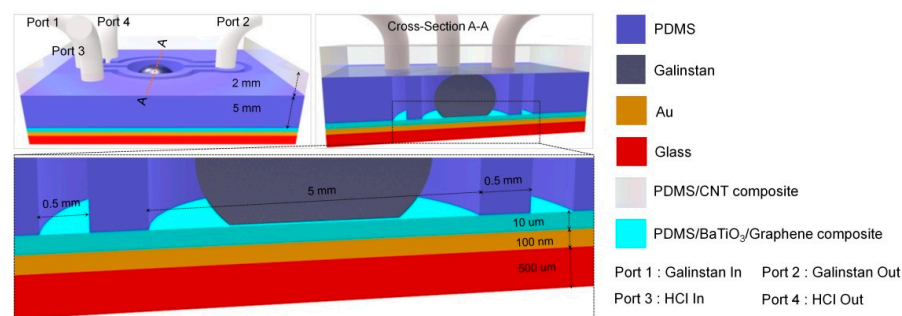


Figure 7. Structure of the reduced Galinstan-based microfluidic energy harvester.

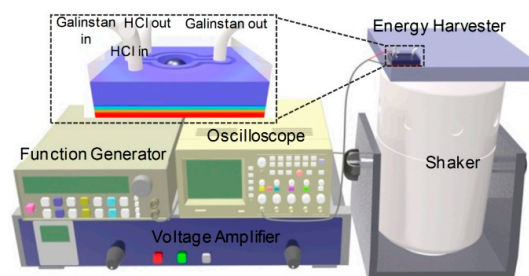


Figure 8. Experiment setup comprising of the reduced Galinstan-based microfluidic energy harvester, function generator, voltage amplifier, shaker and oscilloscope.

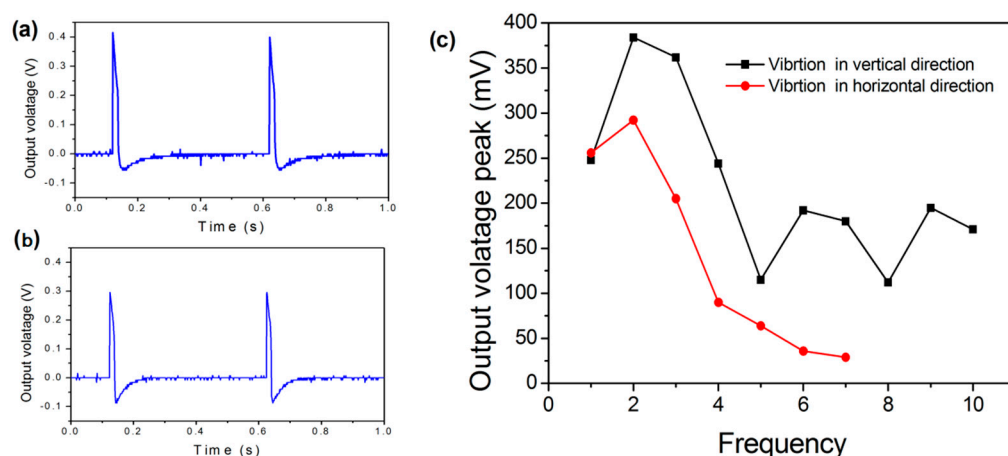


Figure 9. Performance of microfluidic energy harvester. (a) Output voltage of energy harvester after applying a 2 Hz sine wave excitation when it vibrates in the vertical direction. (b) Output voltage of energy harvester after applying a 2 Hz sine wave excitation when it vibrates in the horizontal direction. (c) Output voltage peak of the energy harvester as a function of the frequency of the excitation wave.

3. Conclusions

Due to the oxidation shell, the contact angle of the OGD adhering to a metal and non-metal surface is $\sim 125^\circ$ to $\sim 130^\circ$, and there is no significant difference. Although it has larger contact angle hysteresis of $\sim 149^\circ$ (difference value of receding angle $\sim 6^\circ$ and advancing angle $\sim 155^\circ$), the liquid–solid interfacial area of OGD on the substrate changed almost nothing in the receding step. This means that the capacitance of the liquid–solid interface has a smaller change, which has an influence on increasing the output power density of the liquid metal-based energy harvester [30–32]. The reason is that the Galinstan surface easily oxidized in the air environment adheres to almost any solid surface [42–45]. Therefore, the oxidation surface of Galinstan should be removed to make it be in true liquid phase for increasing the capacitance of the liquid–solid interface. After removing the oxidation surface of Galinstan, the RGD shows super-lyophobic behaviors on non-metal (PDMS) substrate and has smaller contact angle hysteresis of $\sim 17^\circ$ (difference value of receding angle $\sim 138^\circ$ and advancing angle $\sim 155^\circ$). Meanwhile, it exhibits a robust impact effect and has larger liquid–solid interfacial area change. The reason is that the oxidation shell (Ga_2O_3 and Ga_2O) on the surface of Galinstan can be reduced by hydrochloric acid solution and remains in true liquid phase with higher surface tension [42–45]. The larger capacitance change of the liquid–solid interface can increase the output power density of the Galinstan-based energy harvester [30–32]. After characterizing the super-lyophobic behaviors of RGD, the EDLC-based microfluidic energy harvester with reduced Galinstan is used to collect energy from an arbitrary vibration source. The novel device can not only overcome the problem of mercury toxicity and the easy oxidation of Galinstan, but also avoids the evaporation of water in the air environment. We believe that the output power of the new energy harvester can be highly improved after arraying in future work.

4. Experimental Section

4.1. Preparation of Reduced Galinstan

Liquid metal is a pure metal or an alloy with a very low melting point and is in liquid phase at room temperature (or near room temperature). Hg (mercury, melt point: -38.8°C) is the best known liquid metal and remains the only metallic element that is liquid phase at standard temperature and pressure (25°C , 101.3 kPa). In addition, there are three other metallic elements that melt above room temperature: Cs (cesium, melt point: 28.5°C), Ga (gallium, melt point: 29.8°C) and Rb (rubidium, melt point: 39.3°C). Unfortunately, Cs is extremely reactive, Rb is radioactive, and the surface of Ga is easy oxidized. Actually,

these three metals are solid at room temperature due to their melt point, which is slightly higher than 25 °C. Although Hg is the most well-known liquid metal, its toxicity and higher vapor pressure pose a challenge for its widespread use in applications. Except the above metals, there are some alloys which are in liquid phase at room temperature. NaK alloy (sodium–potassium, 22 wt% sodium and 78 wt% potassium) is usually liquid from 12.6 °C to 785 °C. However, NaK is highly reactive with water and may catch fire when exposed to air. Recently, gallium-based liquid metal alloy has emerged as a replacement of the previously employed toxic mercury or the reactive NaK due to the non-toxicity and low reactivity of its component metals. Typical gallium-based liquid metal is EGaIn (eutectic gallium–indium) and Galinstan (Ga–In–Sn alloy).

The general composition of EGaIn is 75.5 wt% gallium and 24.5 wt%. Galinstan is commercially available (Geratherm Medical AG, Geschwenda, Germany) Ga–In–Sn alloy (68.5 wt%, 21.5 wt%, and 10 wt%) has excellent properties such as non-toxicity, a low melting point (−19 °C), a high electrical conductivity ($3.46 \times 10^6 \text{ S}\cdot\text{m}^{-1}$), a high boiling point (1300 °C), a favorable thermal conductivity ($16.5 \text{ W}\cdot\text{m}^{-1}\cdot\text{K}^{-1}$) and an ultralow vapor pressure, compared with Hg (shown in Table S1 of the Supplementary Material). Based on its favorable properties, Galinstan has been investigated for a variety of applications including microfluidic electronics, stretchable bio-sensors, etc. However, Galinstan is readily oxidized in an air environment, forming a gallium oxide (Ga_2O_3 and Ga_2O) shell on the surface of the material. This causes Galinstan to be viscoelastic and to adhere to almost any surface, which extremely influences the wetting properties of the material. In our study, the oxide layer of Galinstan can be simply removed by using the 16 wt% HCl solution. Firstly, the Galinstan droplet was immersed in the beaker with 16 wt% HCl solution of 5 mL. The oxidation layer was removed instantaneously due to the reduction action. After that, the reduced Galinstan maintained a true liquid phase and was sucked into the syringe through the syringe needle for the following experiment. Another approach is the use of HCl vapor which can be easily generated at ambient condition. Once we added the HCl droplet to the surface of Galinstan droplet, the oxide skin on the Galinstan was quickly removed by the reduction process (shown in Figure S1 of the Supplementary Material).

4.2. Fabrication of Reduced Galinstan-Based Energy Harvester

The device was composed of five parts: glass substrata coated Au (gold) as the bottom conductive plate (Gold thickness: 100 nm, Glass thickness: 0.5 mm), conductive PDMS/CNT (polydimethylsiloxane/carbon-nano-tube) composite as the top conductive plate (thickness: 2 mm, CNT concentration: 60 wt%), PDMS/BaTiO₃ (BaTiO₃ concentration: 60 volume %) composite with 10 wt% Graphene as the dielectric material (dielectric constant: ~31), a coplanar microfluidic channel (the sub-channel and the main-channel) and a Galinstan droplet (~36 µL). The easy oxidation of Galinstan restricts its impact effect, thereby affecting the performance of the microfluidic energy harvester. However, Galinstan can be maintained in true liquid phase when the sub-channel is filled with 37 wt% HCl solution. Due to the high gas permeability of PDMS, HCl vapor can permeate through the PDMS wall (between the sub-channel and the main channel) and reduce gallium oxide, which is illustrated in Figure 7 [42]. The PDMS wall thickness is also one of the important parameters, which determines the diffusion time of HCl vapor. This parameter has been optimized in our previous work. In order to prevent leakage of the HCl vapor into the air, parylene (PPX) was coated on both surfaces using a chemical vapor deposition technique. After fabrication, the experiment setup comprising of a function generator, voltage amplifier, shaker and oscilloscope was used to characterize the behavior of the energy harvester, as shown in Figure 8.

Supplementary Materials: The following are available online at <https://www.mdpi.com/article/10.3390/polym14173633/s1>, Figure S1: Photographs of oxidized Galinstan before and after closing to the HCl droplet, Figure S2: Sequential photographs of the RGD on PDMS and Au substrate (initially touching–fully wetting, Table S1: Properties of gallium-based liquid metal, Ga, Hg, NaK, Cs and Rb, Table S2: Summary of properties for liquid metal-based energy harvesters, Video S1: The behaviors

of the RGD after release from a height of 20 mm and impacting on PDMS surface, Video S2: The behaviors of the RGD after release from a height of 20 mm and impacting on Au surface, Video S3: The video shows the vibration of the RGD in vertical direction, Video S4: The video shows the vibration of the RGD in horizontal direction.

Author Contributions: Conceptualization, H.C. and G.L.; methodology, A.Z.; software, L.H.; validation, S.H., Y.J. and J.D.; formal analysis, H.C.; investigation, S.H.; resources, A.Z.; data curation, Y.J.; writing—original draft preparation, G.L.; writing—review and editing, G.L.; visualization, L.H.; supervision, A.Z.; project administration, J.D.; funding acquisition, G.L. All authors have read and agreed to the published version of the manuscript.

Funding: This study was supported by the Natural Science Foundation of China (Grant No. 11802149) and the Natural Science Foundation of Ningbo city, China (Grant No. 2021J123). It was also supported by K.C. Wong Magna Fund of Ningbo University.

Institutional Review Board Statement: Not applicable.

Informed Consent Statement: Not applicable.

Data Availability Statement: The data presented in this study are available on request from the corresponding author.

Conflicts of Interest: The authors declare no conflict of interest.

References

1. Yu, J.; Ma, T. Triboelectricity-based self-charging droplet capacitor for harvesting low-level ambient energy. *Nano Energy* **2020**, *74*, 104795. [[CrossRef](#)]
2. Wu, X.; Li, G.; Lee, D.-W. A novel energy conversion method based on hydrogel material for self-powered sensor system applications. *Appl. Energy* **2016**, *173*, 103–110. [[CrossRef](#)]
3. Wu, H.; Mendel, N.; van der Ham, S.; Shui, L.; Zhou, G.; Mugele, F. Charge Trapping-Based Electricity Generator (CTEG): An Ultrarobust and High Efficiency Nanogenerator for Energy Harvesting from Water Droplets. *Adv. Mater.* **2020**, *32*, 2001699. [[CrossRef](#)] [[PubMed](#)]
4. Wijewardhana, K.R.; Shen, T.-Z.; Song, J.-K. Energy harvesting using air bubbles on hydrophobic surfaces containing embedded charges. *Appl. Energy* **2017**, *206*, 432–438. [[CrossRef](#)]
5. Liang, J.; Liao, W.-H. Impedance Modeling and Analysis for Piezoelectric Energy Harvesting Systems. *IEEE/ASME Trans. Mechatron.* **2011**, *17*, 1145–1157. [[CrossRef](#)]
6. Hua, R.; Liu, H.; Yang, H.; Wang, Y.; Ferrante, J. A nonlinear interface integrated lever mechanism for piezoelectric footstep energy harvesting. *Appl. Phys. Lett.* **2018**, *113*, 053902. [[CrossRef](#)]
7. Helseth, L.E.; Guo, X.D. Contact Electrification and Energy Harvesting Using Periodically Contacted and Squeezed Water Droplets. *Langmuir* **2015**, *31*, 3269–3276. [[CrossRef](#)]
8. Al Ahmad, M.; Jabbour, G. Electronically droplet energy harvesting using piezoelectric cantilevers. *Electron. Lett.* **2012**, *48*, 647–649. [[CrossRef](#)]
9. Krupenkin, T.N.; Taylor, J.A. Reverse electrowetting as a new approach to high-power energy harvesting. *Nat. Commun.* **2011**, *2*, 448. [[CrossRef](#)]
10. Moon, J.K.; Jeong, J.; Lee, D.; Pak, H.K. Electrical power generation by mechanically modulating electrical double layers. *Nat. Commun.* **2013**, *4*, 1487. [[CrossRef](#)]
11. Kong, W.; Cao, P.; He, X.; Yu, L.; Ma, X.; He, Y.; Lu, L.; Zhang, X.; Deng, Y. Ionic liquid based vibrational energy harvester by periodically squeezing the liquid bridge. *RSC Adv.* **2014**, *4*, 19356–19361. [[CrossRef](#)]
12. Hsu, T.-H.; Taylor, J.A.; Krupenkin, T.N. Energy harvesting from aperiodic low-frequency motion using reverse electrowetting. *Faraday Discuss.* **2017**, *199*, 377–392. [[CrossRef](#)] [[PubMed](#)]
13. Conner, C.; de Visser, T.; Loessberg, J.; Sherman, S.; Smith, A.; Ma, S.; Napoli, M.T.; Pennathur, S.; Weld, D. Energy Harvesting with a Liquid-Metal Microfluidic Influence Machine. *Phys. Rev. Appl.* **2018**, *9*, 044008. [[CrossRef](#)]
14. Adhikari, P.R.; Tasneem, N.T.; Reid, R.C.; Mahbub, I. Electrode and electrolyte configurations for low frequency motion energy harvesting based on reverse electrowetting. *Sci. Rep.* **2021**, *11*, 1–13. [[CrossRef](#)]
15. Chen, G.; Liu, X.; Li, S.; Dong, M.; Jiang, D. A droplet energy harvesting and actuation system for self-powered digital microfluidics. *Lab Chip* **2018**, *18*, 1026–1034. [[CrossRef](#)]
16. Lin, Z.-H.; Cheng, G.; Lee, S.; Pradel, K.C.; Wang, Z.L. Harvesting Water Drop Energy by a Sequential Contact-Electrification and Electrostatic-Induction Process. *Adv. Mater.* **2014**, *26*, 4690–4696. [[CrossRef](#)]
17. Zhu, G.; Su, Y.; Bai, P.; Chen, J.; Jing, Q.; Yang, W.; Wang, Z.L. Harvesting Water Wave Energy by Asymmetric Screening of Electrostatic Charges on a Nanostructured Hydrophobic Thin-Film Surface. *ACS Nano* **2014**, *8*, 6031–6037. [[CrossRef](#)]

18. Kwon, S.-H.; Park, J.; Kim, W.K.; Yang, Y.; Lee, E.; Han, C.J.; Park, S.Y.; Lee, J.; Kim, Y.S. An effective energy harvesting method from a natural water motion active transducer. *Energy Environ. Sci.* **2014**, *7*, 3279–3283. [[CrossRef](#)]
19. Helseth, L.E.; Guo, X.D. Hydrophobic polymer covered by a grating electrode for converting the mechanical energy of water droplets into electrical energy. *Smart Mater. Struct.* **2016**, *25*, 045007. [[CrossRef](#)]
20. Su, Y.; Wen, X.; Zhu, G.; Yang, J.; Chen, J.; Bai, P.; Wu, Z.; Jiang, Y.; Wang, Z.L. Hybrid triboelectric nanogenerator for harvesting water wave energy and as a self-powered distress signal emitter. *Nano Energy* **2014**, *9*, 186–195. [[CrossRef](#)]
21. Pu, X.; Guo, H.; Chen, J.; Wang, X.; Xi, Y.; Hu, C.; Wang, Z.L. Eye motion triggered self-powered mechnosensational communication system using triboelectric nanogenerator. *Sci. Adv.* **2017**, *3*, e1700694. [[CrossRef](#)] [[PubMed](#)]
22. Li, C.; Yin, Y.; Wang, B.; Zhou, T.; Wang, J.; Luo, J.; Tang, W.; Cao, R.; Yuan, Z.; Li, N.-W.; et al. Self-Powered Electrospinning System Driven by a Triboelectric Nanogenerator. *ACS Nano* **2017**, *11*, 10439–10445. [[CrossRef](#)] [[PubMed](#)]
23. Liu, X.; Zhao, K.; Wang, Z.L.; Yang, Y. Unity Convoluted Design of Solid Li-Ion Battery and Triboelectric Nanogenerator for Self-Powered Wearable Electronics. *Adv. Energy Mater.* **2017**, *7*, 1701629. [[CrossRef](#)]
24. Yu, H.; He, X.; Ding, W.; Hu, Y.; Yang, D.; Lu, S.; Wu, C.; Zou, H.; Liu, R.; Lu, C.; et al. A Self-Powered Dynamic Displacement Monitoring System Based on Triboelectric Accelerometer. *Adv. Energy Mater.* **2017**, *7*, 1700565. [[CrossRef](#)]
25. He, X.; Zi, Y.; Yu, H.; Zhang, S.L.; Wang, J.; Ding, W.; Zou, H.; Zhang, W.; Lu, C.; Wang, Z.L. An ultrathin paper-based self-powered system for portable electronics and wireless human-machine interaction. *Nano Energy* **2017**, *39*, 328–336. [[CrossRef](#)]
26. Yang, Z.; Halvorsen, E.; Dong, T. Electrostatic Energy Harvester Employing Conductive Droplet and Thin-Film Electret. *J. Microelectromech. Syst.* **2014**, *23*, 315–323. [[CrossRef](#)]
27. Deng, H.; Zhao, Z.; Jiao, C.; Ye, J.; Zhao, S.; Ma, M.; Zhong, X. A Liquid-Metal-Based Freestanding Triboelectric Generator for Low-Frequency and Multidirectional Vibration. *Front. Mater.* **2021**, *8*, 692273. [[CrossRef](#)]
28. Li, G.; Sun, F.; Chen, H.; Jin, Y.; Zhang, A.; Du, J. High-Efficiency Large-Area Printed Multilayer Liquid Metal Wires for Stretchable Biomedical Sensors with Recyclability. *ACS Appl. Mater. Interfaces* **2021**, *13*, 56961–56971. [[CrossRef](#)]
29. West, D.; Taylor, J.A.; Krupenkin, T. Alternating Current Liquid Metal Vortex Magnetohydrodynamic Generator. *Eng. Convers. Manag.* **2020**, *223*, 113223. [[CrossRef](#)]
30. Vallem, V.; Roosa, E.; Ledin, T.; Jung, W.; Kim, T.I.; Rashid-Nadimi, S.; Kiani, A.; Dickey, M.D. A Soft Variable-Area Electrical-Double-Layer Energy Harvester. *Adv. Mater.* **2021**, *33*, 2103142. [[CrossRef](#)]
31. Jeon, J.; Chung, S.K.; Lee, J.-B.; Doo, S.J.; Kim, D. Acoustic wave-driven oxidized liquid metal-based energy harvester. *Eur. Phys. J. Appl. Phys.* **2018**, *81*, 20902. [[CrossRef](#)]
32. Hsu, T.-H.; Manakasettharn, S.; Taylor, J.A.; Krupenkin, T. Bubbler: A Novel Ultra-High Power Density Energy Harvesting Method Based on Reverse Electrowetting. *Sci. Rep.* **2015**, *5*, 16537. [[CrossRef](#)] [[PubMed](#)]
33. Dickey, M.D. Stretchable and Soft Electronics using Liquid Metals. *Adv. Mater.* **2017**, *29*, 1606425. [[CrossRef](#)] [[PubMed](#)]
34. Li, G.; Du, J.; Zhang, A.; Lee, D.-W. Electrochemically controllable actuation of liquid metal droplets based on Marangoni effect. *J. Appl. Phys.* **2019**, *126*, 084505. [[CrossRef](#)]
35. Matsuhisa, N.; Chen, X.; Bao, Z.; Someya, T. Materials and structural designs of stretchable conductors. *Chem. Soc. Rev.* **2019**, *48*, 2946–2966. [[CrossRef](#)] [[PubMed](#)]
36. Li, G.; Parmar, M.; Lee, D.-W. An oxidized liquid metal-based microfluidic platform for tunable electronic device applications. *Lab Chip* **2015**, *15*, 766–775. [[CrossRef](#)] [[PubMed](#)]
37. Jeong, S.H.; Hagman, A.; Hjort, K.; Jobs, M.; Sundqvist, J.; Wu, Z. Liquid alloy printing of microfluidic stretchable electronics. *Lab Chip* **2012**, *12*, 4657–4664. [[CrossRef](#)] [[PubMed](#)]
38. Li, G.; Du, J.; Zhang, A.; Lee, D. Artificial Heart Based on Electrically Controlled Non-Toxic Liquid Metal Pump. *Adv. Eng. Mater.* **2019**, *21*, 1900381. [[CrossRef](#)]
39. Jeong, S.H.; Hjort, K.; Wu, Z. Tape Transfer Printing of a Liquid Metal Alloy for Stretchable RF Electronics. *Sensors* **2014**, *14*, 16311–16321. [[CrossRef](#)]
40. Jeong, S.; Hjort, K.; Wu, Z. Tape Transfer Atomization Patterning of Liquid Alloys for Microfluidic Stretchable Wireless Power Transfer. *Sci. Rep.* **2015**, *5*, srep08419. [[CrossRef](#)]
41. Zhang, Q.; Gao, Y.; Liu, J. Atomized spraying of liquid metal droplets on desired substrate surfaces as a generalized way for ubiquitous printed electronics. *Appl. Phys. A* **2014**, *116*, 1091–1097. [[CrossRef](#)]
42. Li, G.; Parmar, M.; Kim, D.; Lee, J.-B.; Lee, D.-W. PDMS based coplanar microfluidic channels for the surface reduction of oxidized Galinstan. *Lab Chip* **2014**, *14*, 200–209. [[CrossRef](#)] [[PubMed](#)]
43. Li, G.; Wu, X.; Lee, D.-W. Selectively plated stretchable liquid metal wires for transparent electronics. *Sens. Actuators B Chem.* **2015**, *221*, 1114–1119. [[CrossRef](#)]
44. Li, G.; Lee, D.-W. An advanced selective liquid-metal plating technique for stretchable biosensor applications. *Lab Chip* **2017**, *17*, 3415–3421. [[CrossRef](#)]
45. Li, G.; Wu, X.; Lee, D.-W. A galinstan-based inkjet printing system for highly stretchable electronics with self-healing capability. *Lab Chip* **2016**, *16*, 1366–1373. [[CrossRef](#)]
46. Zuo, L.; Scully, B.; Shestani, J.; Zhou, Y. Design and characterization of an electromagnetic energy harvester for vehicle suspensions. *Smart Mater. Struct.* **2010**, *19*, 045003. [[CrossRef](#)]
47. Yang, B.; Lee, C.; Kee, W.L.; Lim, S.-P. Hybrid energy harvester based on piezoelectric and electromagnetic mechanisms. *J. Micro/Nanolithogr. MEMS MOEMS* **2010**, *9*, 023002. [[CrossRef](#)]